

1 **Double reservoirs imaged below Great Sitkin Volcano,**
2 **Alaska, explain the migration of volcanic seismicity**

3 **Xiaotao Yang¹, Diana C. Roman², Matt Haney³, Cody A. Kupres¹**

4 ¹Department of Earth, Atmospheric, and Planetary Sciences, Purdue University, West Lafayette, IN,
5 USA.

6 ²Earth and Planets Laboratory, Carnegie Institution for Science, Washington, DC, USA

7 ³Alaska Volcano Observatory, USGS, Anchorage, AK, USA

8 **Key Points:**

- 9 • The pre- and co-eruptive seismicity below Great Sitkin Volcano, Alaska, shows a
10 strong spatiotemporal migration
- 11 • A new 3-D shear-wave velocity model reveals two crustal low-velocity anomalies
12 that correlate with the migrating seismicity
- 13 • We propose a six-stage eruption cycle involving two magma reservoirs to explain
14 the long-term and short-term seismicity patterns

Corresponding author: Xiaotao Yang, xyang@purdue.edu

Abstract

Volcanic seismicity provides essential insights into the behavior of an active volcano across multiple time scales. However, to understand how magma moves as an eruption evolves, better knowledge of the geometry and physical properties of the magma plumbing system is required. In this study, using full-wave ambient noise tomography, we image the 3-D crustal shear-wave velocity structure below Great Sitkin Volcano in the central Aleutian Arc. The new velocity model reveals two low-velocity anomalies, which correlate with the migration of volcanic seismicity. With a partial melt of up to about 30%, these low-velocity anomalies are characterized as mushy magma reservoirs. We propose a six-stage eruption cycle to explain the migration of seismicity and the alternating eruption of two reservoirs with different recharging histories. The findings in this study have broad implications for the dynamics of magma plumbing systems and the structural control of eruption behaviors.

Plain Language Summary

Understanding magma accumulation and transport systems below active volcanoes is essential for predicting eruption behavior and assessing the potential hazards. The distribution of earthquakes can partly be used to infer the development of magmatic activity at different times. However, to understand how magma moves at different stages of an eruption cycle, better knowledge of what the magma plumbing system looks like is necessary. In this study, we use an advanced seismic imaging method to construct the 3-D crustal shear-wave velocity structure below Great Sitkin Volcano in the central Aleutian Arc. The new velocity model reveals two crustal magma reservoirs, which correlate with the migration of seismicity. We propose a six-stage eruption cycle to explain the evolution of seismicity in space and time across the island and the alternating eruption of two reservoirs. The findings in this study help to understand better the control of eruption behaviors by the underlying magma plumbing system at active volcanoes.

1 Introduction

Magma plumbing systems of active volcanoes consist of magma storage reservoirs and conduits for transportation of magma to the surface (e.g., Tibaldi, 2015; Chaussard et al., 2013). The geometry and dynamics of magma plumbing systems play an essential role in controlling the eruption behavior. Magma plumbing systems possess a wide range of complexity in terms of the connection and interaction between multiple magma chambers (e.g., Tibaldi, 2015; Huang et al., 2015; Kiser et al., 2021), the lateral offset between reservoirs and the edifice (e.g., Tibaldi, 2015; Lerner et al., 2020), the geochemical evolution of the magma (e.g., Spera, 2004), and the development of eruptive activity in an eruption cycle (e.g., Tibaldi, 2015; Chaussard et al., 2013; Roman & Cashman, 2018; Paulatto et al., 2022). Among these complexities, it is important to understand how magma moves in space and time during an eruption and between eruptions and what controls this process. We address these questions by investigating Great Sitkin Volcano in central Aleutian Arc in Alaska (Figure 1a) (e.g., Miller et al., 1998; Waythomas et al., 2003), which erupted on 26 May 2021 with ongoing effusive lava flows as of the time of writing (Global Volcanism Program, 2022a). Great Sitkin Volcano is an oval-shaped stratovolcano with a collapsed caldera (Waythomas et al., 2003) and an edifice aperture of about 8 by 11 km (Figure 1a) (Miller et al., 1998). The volcanic rocks are dominantly andesites to basaltic andesites (Miller et al., 1998; Waythomas et al., 2003). The ongoing eruption started as an explosive eruption on 26 May 2021 and was preceded by multiple phreatic explosions between June 2018 and February 2019. The 26 May 2021 eruption was followed by a dome emplacement that peaked in growth rate during August through September (Global Volcanism Program, 2022b, 2022a; Marchese & Genzano, 2022).

Seismic activity at volcanoes helps to reveal the evolution of the eruption activity (e.g., Power et al., 2004; Roman et al., 2004; Scandone et al., 2007; Pesicek et al., 2008; Roman & Cashman, 2018). At Great Sitkin, volcanic earthquakes (5/1/2020-9/5/2022) are primarily concentrated along an NW-SE trending zone (Figure 1a). This seismic zone delineates an inverse-V shape in depth, with the shallowest earthquakes below the caldera summit and the 2021 eruption vent (Figure 1a and b). Locations of the pre- and co-eruptive seismicity suggest the migration of magmatic activity (Figure 1b-d). Approximately 24 hours before the 26 May 2021 eruption, seismicity started to increase abruptly (Figure 1c) with a swarm of earthquakes northwest of the edifice (swarm-1 in Figure 1a-b). About two months later, a second earthquake swarm (swarm-2) occurred further to the southeast. Interestingly, about one year after the initial eruption, there was another earthquake swarm (swarm-3) northwest of the edifice, generally at greater depth than swarm-1 earthquakes. In the longer term (Figure 1d), there was an earthquake cluster in early 2002 through 2004 southeast of the edifice (Pesicek et al., 2008). Pesicek et al. (2008) and Power et al. (2004) argue that this cluster of volcano-tectonic earthquakes and the co-occurring long-period events are evidence of a magma intrusion. This elevated seismicity (Figure 1d) suggests that the reservoir to the southeast of the volcano edifice may have begun recharging as early as 2002, reaching its peak in 2020. In contrast, to the northwest of the volcano edifice, there was a slight increase in seismicity in 2018, followed by a relatively seismically quiet period in 2020 until the day before the eruption (Global Volcanism Program, 2022b). However, it is not clear how the migration of seismicity is linked to the geometry and dynamics of the magma plumbing system.

We investigate structural controls of the spatial-temporal migration of seismicity at Great Sitkin Volcano and the associated eruption stages. We construct a 3-D shear-wave velocity model for the upper 6 km of the crust below sea level (BSL) under Great Sitkin, using a full-wave ambient noise tomography method. The new shear-wave velocity model reveals two low-velocity anomalies at 1.5-4.5 km BSL and 3-6 km BSL to the southeast and northwest of the volcano edifice, respectively. These low-velocity anomalies correspond to up to approximately 30% partial melts and are thus characterized as mushy magma

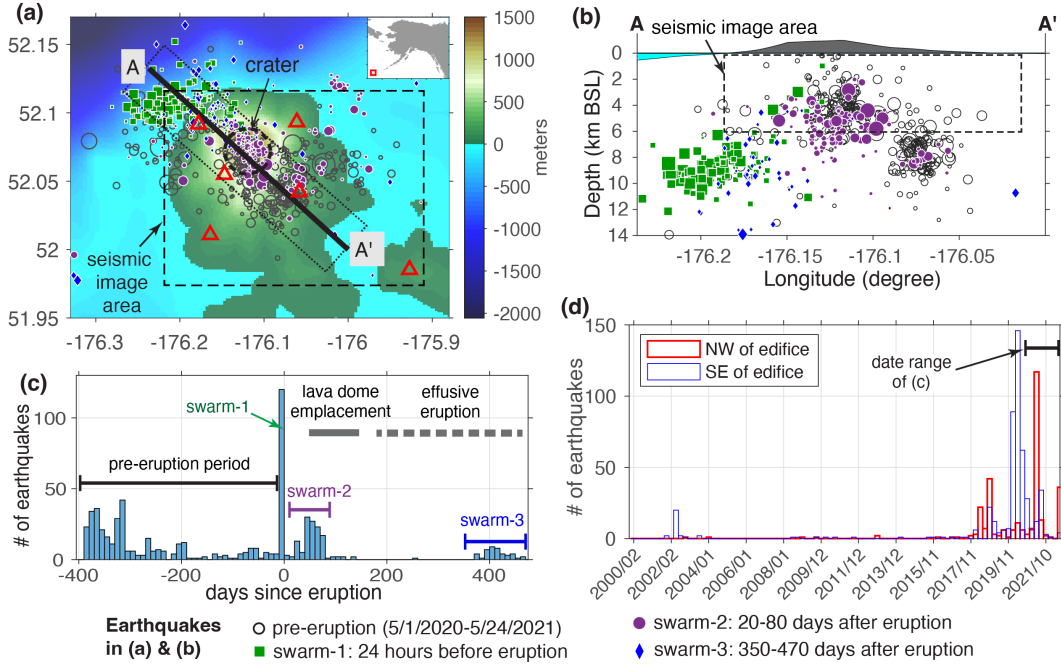


Figure 1. Distribution of earthquakes around Great Sitkin Volcano between different time periods. (a) Earthquake epicenters (magnitude ≥ 0) from the USGS Comprehensive Earthquake Catalog (ComCat) (U.S. Geological Survey, 2022) from May 2020 to September 2022, scaled by magnitude. The main explosive eruption occurred at 5:04 UTC on 26 May 2021. The pre-eruption earthquakes (5/1/2020-5/24/2021) are shown as open circles. Swarm-1 (green squares) refers to earthquakes within approximately 24 hours before the 26 May 2021 eruption. Swarm-2 (purple dots) includes earthquakes 10-100 days after the initial eruption. Swarm-3 (blue diamonds) contains earthquakes 300-470 days after the initial eruption. Triangles are seismic stations from the Alaska Volcano Observatory network (network code: AV) used in this study (Alaska Volcano Observatory/USGS, 1988). The dashed box shows the seismic imaging area. (b) Depth distribution of the earthquakes along profile A-A' highlighting the three earthquake swarms. The dashed box shows the seismic imaging area. BSL: below sea level. (c) Histogram with 10-day bins showing the variation of seismicity within 2 km from profile A-A', shown as the dotted box in (a). The three earthquake swarms are labeled along with the key development phases of the eruption. (d) Histograms with 90-day bins showing the longer-term variations of seismicity between 1/1/2000 and 9/5/2022 to the northwest (thick red bars) and southeast (thin blue bars) of the volcano edifice. The earthquakes below the crater atop the edifice, with the lateral extent defined by the dashed circle in (a), are excluded in (d).

92 reservoirs. We propose a six-stage eruption cycle to explain the spatiotemporal migration
 93 of the volcanic seismicity at Great Sitkin.

94 2 Data and Methods

95 2.1 Empirical Green's functions

96 Empirical Green's functions between two seismic stations can be retrieved from the
 97 cross-correlations of ambient noise waveforms. We use the *SeisGo* Python toolbox to down-
 98 load the continuous seismic waveforms and compute the cross-correlations (Yang et al.,

2022). The Alaska Volcano Observatory operates six broadband seismic stations on Great Sitkin Island and nearby Igitkin Island (network code: AV; triangles in Figure 1a) (Alaska Volcano Observatory/USGS, 1988). We download the vertical continuous waveforms from these stations between 7/1/2019 and 8/1/2020 from the IRIS Data Management Center. We downsample the waveforms at the rate of 20 Hz, followed by the removal of the instrument responses.

We slice the continuous waveforms into 4-hour segments with a step of 2 hours and normalize the amplitude spectrum of each segment using the moving average method, as described by Bensen et al. (2007). We attempt to further eliminate transient signals by discarding segments with peak amplitudes greater than 10 times the standard deviation of all segments within each downloaded 3-day block, following Jiang and Denolle (2020). We then compute the cross-correlations in the frequency domain following Viens et al. (2017). We calculate the stacks of the cross-correlations across the entire duration and within each 30-day window to provide uncertainties of the phase delay measurements in Section 2.2. The empirical Green's functions are computed as the negative time derivative of the cross-correlations.

2.2 Full-wave ambient noise tomography

We apply the full-wave ambient noise tomography method, which involves full-wavefield simulation, to invert for the velocity perturbations using finite-frequency kernels (e.g., Gao & Shen, 2012, 2014; Yang & Gao, 2018, 2020). The tomography method accounts for the cross-dependence of Rayleigh waves to both P and S wave velocities (Z. Zhang & Shen, 2008). We first simulate the wave propagation in the 3-D spherical Earth using a nonstaggered-grid, finite-difference method (W. Zhang et al., 2012), with a grid spacing of 0.001 and 0.0013 degrees in the latitudinal and longitudinal directions, respectively. The vertical grid spacing increases with depth from 0.037 km at the surface to 0.022 km at the depth of 28 km. We use the global velocity model by Shapiro and Ritzwoller (2002) as the reference model. We then measure the Rayleigh wave phase delays between the synthetics and the observed empirical Green's functions through cross-correlations in eight overlapping period ranges, including 0.6-1s, 0.8-1.25s, 1-1.5s, 1.25-1.8s, 1.5-2s, 1.8-2.5s, 2-3s, and 2.5-3.5s. Before measuring the phase delays, we discard empirical Green's functions with signal-to-noise ratios below 3. The phase delay measurements with correlation coefficients ≥ 0.6 are used in the kernel calculation and inversion. The reference velocity model is progressively updated for four iterations until major velocity features converge to achieve the final model.

3 Results: Shear-Wave Velocity Model

The shear-wave velocity model reveals two low-velocity features at different depths aligning in the northwest-southeast direction (L1 and L2 in Figure 2). At a depth of 2 km (Figure 2a-b), we observe a prominent, localized low-velocity feature (1-1.2 km/s) beneath station GSMY (anomaly L1). This anomaly extends down to about 3-4 km BSL, where the velocity is about 1.5-2.1 km/s (Figure S1a). At greater depths (Figures 2c and S1a), the velocity generally decreases toward the northwest with a low-velocity anomaly of 2.2-2.6 km/s in the broad region below station GSSP (anomaly L2). The vertical velocity cross-section A-A' (NW-SE across the island) shows the separation of these two low-velocity anomalies (with up to -10% perturbations) in both lateral and vertical directions (Figure 2d). Both of these two low-velocity anomalies, particularly L1, appear to be dipping to the northwest (Figure 2d), though the top of the L1 anomaly is not well-constrained. The NW-SE alignment of these two low-velocity anomalies is consistent with the location of the NW-SE trending seismic zone (Figures 1a and 2a-c). The cross-sections along profiles B-B' and C-C' show that the L1 low-velocity anomaly is localized in the SW-NE direction and is bounded by higher velocities extending down to at least 6 km BSL, below which our resolution is dramatically decreased, as described below.

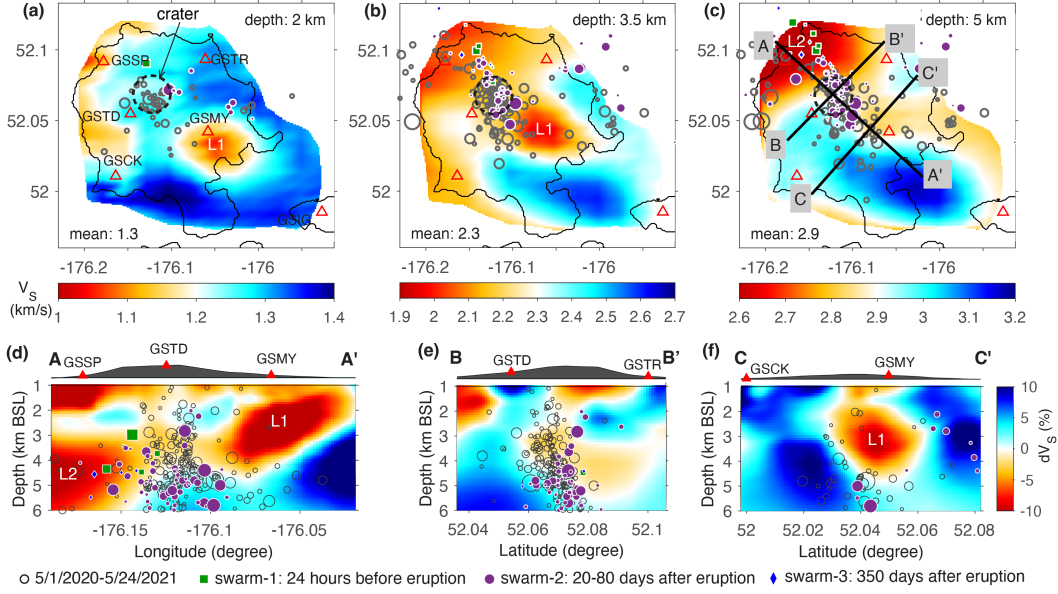


Figure 2. Shear-wave velocity model of Great Sitkin. (a)-(c) Velocity depth slices at 2 km, 3.5 km, and 5 km BSL, respectively. The average velocity at each depth is given in the lower-left corner of each panel. The triangles are AV seismic stations. Earthquakes are projected about ± 1 km around the slice depth, scaled by magnitudes. Gray circles are earthquakes between 5/1/2020 and 5/24/2021. Earthquake swarm-1 (green squares), swarm-2 (purple dots), and swarm-3 (blue diamonds) are shown for reference, color-coded the same as Figure 1a. The dashed circle marks the extent of the crater atop the volcano edifice. L1 and L2 label the two key low-velocity features. (d)-(f) Vertical cross-sections of the shear-wave velocity model at 1-6 km BSL, showing the velocity perturbations relative to the average velocity at each depth. Since the absolute velocities span across a wide range from 1 km/s to about 3.5 km/s (Figure S1), we use perturbations to highlight the velocity anomalies. Earthquakes are projected within about 2 km away from each profile, color-coded as in (a)-(c). See panel (c) for the profile locations.

149 The checkerboard resolution tests (Figure S3) and model recovery tests (Figure S4)
 150 suggest that our best resolution is for the depth range of 2-5 km BSL, degrading dramatically
 151 at greater depths. We can resolve the geometry of velocity anomalies with a horizontal scale
 152 of >3.5 km and a vertical scale of > 2 km. In addition, L1 can be resolved much better than
 153 L2 (Figure S4). In later sections, when analyzing the absolute velocities or perturbation
 154 amplitudes, we focus more on the L1 anomaly. See Text S1 in the supplement for a detailed
 155 resolution analysis.

156 4 Discussion

157 4.1 Correlation with seismicity

158 The key features in the new velocity model show a strong correlation with the earth-
 159 quake activity below Great Sitkin Island. The earthquakes from 5/1/2020 to 9/5/2022 are
 160 concentrated between these two low-velocity anomalies mainly at the depth of > 2 km BSL
 161 (L1 and L2 in Figure 2d). The centers of both L1 and L2 anomalies are relatively aseismic
 162 (Figure 2d and f). Below the depth of 4 km, the earthquakes are concentrated along rela-
 163 tively large velocity gradients (Figure 2d). This concentration pattern has been observed at
 164 other active volcanoes, such as Mount St. Helens Volcano in the Cascadia volcanic arc (e.g.,

165 Barker & Malone, 1991; Kiser et al., 2016), Mount Spurr Volcano in southwestern Alaska
 166 (Power et al., 1998), the Hawaiian volcanoes (Lin et al., 2014), Redoubt Volcano in Alaska
 167 (Benz et al., 1996), Stromboli Volcano in Italy (Patanè et al., 2017), Mount Rainier Volcano
 168 in Cascadia (Flinders & Shen, 2017), and the Gakkel Ridge volcanic complex (Korger &
 169 Schlindwein, 2014). The occurrence of earthquakes along velocity gradients below volcanic
 170 areas is commonly attributed to the stress concentration at structural boundaries result-
 171 ing from magma movement or dike intrusion (e.g., Korger & Schlindwein, 2014; Barker &
 172 Malone, 1991; Roman et al., 2004; Kiser et al., 2016).

173 The earthquake swarms before and after the 26 May 2021 initial eruption provides
 174 insights into the eruption dynamics. Occurring right before the eruption, swarm-1 earth-
 175 quakes may delineate the magma pathway (with a relatively fast ascent rate) for the initial
 176 eruption, suggesting it was sourced from the L2 reservoir. Swarm-2 earthquakes occurred
 177 during the dome emplacement period (late July 2021 through November 2021; Figure 1c),
 178 primarily along the velocity gradient at the bottom of the L1 anomaly and below the edi-
 179 fice. This spatiotemporal coincidence indicates that the L1 anomaly may be linked to the
 180 dome emplacement. The seismicity at a shallower depth (i.e., < 2 km BSL) likely delineates
 181 shallow magma conduits, which seem to be shared by swarm-1 and swarm-2 (Figure 1b).
 182 However, the detailed geometry and velocity of the shallow conduit are not resolvable in our
 183 model. The distinct difference in the inferred intrusion timelines between the southeast and
 184 the northwest of the edifice is coincident with the spatial separation of the two low-velocity
 185 anomalies (L1 and L2) below these two regions.

186 **4.2 Double magma reservoirs**

187 There are multiple mechanisms that can reduce shear-wave velocities at active volca-
 188 noes, including high-temperature anomalies (e.g., Kern et al., 2001), volatiles (water and
 189 gas) (e.g., Ito, 1990; Chu et al., 2010; Christensen & Stanley, 2003), and partial melts (e.g.,
 190 Avellaneda, 1987; Berryman, 1998; Norris, 1985; Takei, 2002; Paulatto et al., 2022). Con-
 191 sidering the surface heat flow and the distribution of geothermal features at Great Sitkin
 192 Island, the contributions from temperature anomalies to the L1 and L2 low-velocity anom-
 193 alies should be minor (see Text S2 in the supplement). Water and gas are likely to play an
 194 important role in reducing the shear-wave velocities, though the exact contribution is not
 195 well constrained with the current data on water content and gas emissions (e.g., Fischer
 196 et al., 2021). On the other hand, partial melts are commonly used to explain seismic low
 197 velocities below active volcanoes (e.g., Lees, 2007; Lin et al., 2014; Power et al., 1998; Jaxy-
 198 bulatov et al., 2014; Kiser et al., 2016; Ward et al., 2017; Delph et al., 2017; Paulatto et al.,
 199 2022). With the ongoing eruption of the Great Sitkin Volcano, it is reasonable to assume
 200 partial melts as the dominant factor responsible for the velocity reduction of the L1 and L2
 201 anomalies.

202 The melt fraction estimates for L1 and L2 low-velocity anomalies suggest that they
 203 are mushy magma reservoirs with up to approximately 30% partial melts. At Great Sitkin,
 204 the volcanic deposits are dominantly andesite and basaltic andesite (Miller et al., 1998;
 205 Loewen, 2021). We compute the melt fractions following the workflow and computer codes
 206 by Paulatto et al. (2022) using the Self-Consistent Scheme (Figure S5a) (e.g., Berryman,
 207 1998; Paulatto et al., 2022) and the Differential Effective Medium (Figure S5b) (e.g., Norris,
 208 1985; Avellaneda, 1987; Paulatto et al., 2022) methods. We use velocities for crystal and
 209 molten andesite based on the experimental data by Christensen and Stanley (2003), Ueki
 210 and Iwamori (2016), and Takei (2002) (see Text S3 in the supplement for key parameters).
 211 The estimated melt fractions are about 0.23 ± 0.1 and about 0.11 ± 0.05 for the L1 and L2
 212 anomalies, respectively. Because of the limited resolution in recovering the synthetic L2
 213 anomaly (Text S1), the uncertainty of the melt fraction for L2 is relatively large. It is worth
 214 noting that these estimates are the upper limits without considering volatiles. Measurements
 215 of the volatile contents from this volcano, as done for other volcanoes along the Aleutian

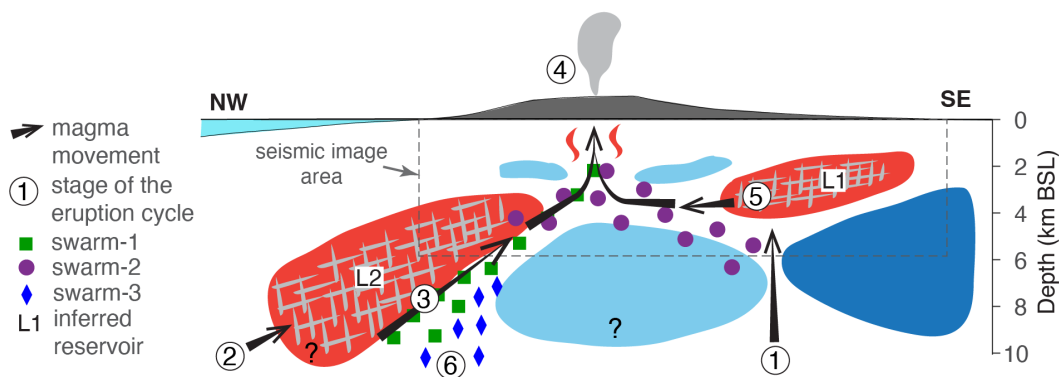


Figure 3. Schematic model showing the six-stage evolution of the 2021-present eruption of the Great Sitkin Volcano. Stage-1: recharge of the L1 reservoir southeast of the edifice. Stage-2: recharge of the L2 reservoir northwest of the edifice. Stage-3: magma ascent and intense fracturing along the lower boundary of the L2 reservoir. Stage-4: explosive eruption with magma primarily from the L2 reservoir. Stage-5: initial dome emplacement with magma primarily from the L1 reservoir. Stage-6: prolonged effusive eruption with magma sourced from the L2 reservoir. The structures within the dashed box are interpreted based on cross-section A-A' (Figure 2d). The question marks denote extrapolated structures that are not constrained by the velocity model.

216 Arc (Fischer et al., 2019, 2021), would help refine the melt estimates. Nevertheless, the
 217 partial melts within the L1 and L2 anomalies are evidence of mushy magma reservoirs.

218 4.3 A six-stage eruption cycle

219 The spatial and temporal migration of seismicity before and after the 26 May 2021
 220 explosive eruption (Figure 1) indicates a complicated eruption cycle, spanning at least 20
 221 years. This eruption cycle likely consists of multiple stages, with added complexity from the
 222 interaction of the two inferred magma reservoirs. Previous studies have proposed several
 223 models to explain multi-stage magma unrest and eruption based on seismicity (e.g., Roman
 224 & Cashman, 2018), surface deformation (e.g., Chaussard et al., 2013), and petrological and
 225 geochemical characteristics (e.g., Spera, 2004; Sparks et al., 2019). However, these models
 226 mostly focus on the vertical migration of magma activity as the eruption cycle evolves.
 227 They cannot explain the bi-modal behaviors of the spatially separated (both laterally and
 228 vertically) magma reservoirs below Great Sitkin Volcano.

229 We propose a six-stage eruption cycle for the 26 May 2021 eruption of the Great Sitkin
 230 Volcano, involving the imaged deep (L2) and shallow (L1) reservoirs (Figure 3). This model
 231 explains the observations from both long- and short-term seismicity (Figure 1) and seismic
 232 velocity structures (Figure 2). It is a refined development of the seismicity and geochemical
 233 evolution models by Spera (2004) and Roman and Cashman (2018). The key development of
 234 our model is the consideration of the interaction and alternation between magma reservoirs.
 235 We describe the six stages of the eruption cycle in the following paragraphs.

236 **Stage-1: Recharge of the shallow reservoir (L1).** At this stage, the shallow
 237 (L1) reservoir southeast of the edifice associated with L1 low-velocity anomaly starts to
 238 recharge, as inferred from the cluster of earthquakes and long-period events (Power et al.,
 239 2004; Pesicek et al., 2008). The magma is likely fed through a nearly vertical pathway down
 240 to at least 12 km, which is the bottom of the earthquake cluster (Pesicek et al., 2008).
 241 Although the resolution is low, this pathway might align with the northwestern boundary of
 242 the relatively high velocities below the L1 reservoir (Figure 2d). The recharge of the

243 L1 reservoir reaches its peak intensity in 2020, corresponding to the elevated seismicity in
 244 late 2020 that decreased in early 2021 (Figure 1d). It is worth noting that Pesicek et al.
 245 (2008) also identified another cluster of earthquakes in March 2002 about 20 km to the west
 246 of the volcano edifice at the depth of >10 km BSL (beyond our study area). Although
 247 they argue that these earthquakes are not volcanic events, we cannot completely rule out
 248 the possibility of magma intrusion at this location based on current constraints. Therefore,
 249 there is a slight chance that there was another magma intrusion in early 2002 further to the
 250 west of the edifice (west of the L2 reservoir).

251 ***Stage-2: Recharge of the deep reservoir (L2).*** About 15-16 years after the initial
 252 recharge of the L1 reservoir, the L2 reservoir west-northwest of the volcano edifice starts
 253 to recharge in late 2017. The recharging process is accompanied by a moderate increase in
 254 earthquake activity lasting through 2020 (Figure 1d). In contrast to the recharge of the L1
 255 reservoir, the lapse is much shorter for the L2 reservoir between the initial recharge and the
 256 eruption. Stages 1 and 2 correspond to the staging phase by Roman and Cashman (2018)
 257 and Spera (2004) but happen at two reservoirs. The current data is insufficient to evaluate
 258 the potential connection of the deep sources feeding these two reservoirs.

259 ***Stage-3: Rapid magma ascent from the L2 reservoir.*** As magma recharge
 260 continues, the pressure within the L2 reservoir slowly builds up to the critical value, causing
 261 intensive fracturing and accelerated ascent of the magma along the lower boundary of the L2
 262 reservoir. This boundary, with fractures, serves as the pathway for magma to quickly move
 263 toward the volcano summit. This magma pathway is delineated by NW-dipping swarm-1
 264 seismic zone and a relatively large seismic velocity gradient (Figure 2d).

265 ***Stage-4: Explosive eruption sourced from the L2 reservoir.*** The intense frac-
 266 turing and magma ascent processes lead to an explosive eruption within 24 hours. Based
 267 on the location of swarm-1 earthquakes, the eruption at this stage is driven mostly by the
 268 magma activity of the L2 reservoir. The drop in seismicity in this region in late 2020, likely
 269 associated with the L1 reservoir, suggests a possible depressurization, such as through in-
 270 flation (e.g., Chaussard et al., 2013). However, more data on surface deformation is needed
 271 to test this hypothesis.

272 ***Stage-5: Dome formation sourced from the L1 reservoir.*** About 2 months
 273 following the initial eruption, an intensive dome emplacement phase begins, accompanied
 274 by a swarm of earthquakes generally below the L1 and L2 reservoirs (swarm-2) (Figure
 275 1c). As implied by the seismicity, the dome emplacement might be driven by the magma
 276 from both reservoirs, explaining the rapid dome growth from July to October 2021 (Global
 277 Volcanism Program, 2022a). However, most of the swarm-2 earthquakes are located below
 278 the L1 reservoir, suggesting that the L1 reservoir dominates the magma activity at this stage.
 279 This stage is an important development compared to previously proposed eruption cycles
 280 (e.g., Roman & Cashman, 2018; Spera, 2004; Chaussard et al., 2013), as it implies dynamic
 281 interaction between the reservoirs. Specifically, the eruption and fast magma transport of
 282 the L2 reservoir may have created fractures that helped to unseal the L1 reservoir. The
 283 magma moves toward the conduits even when the pressure is below the critical point with
 284 relatively low seismicity. This explains why the dome emplacement is more effusive than
 285 explosive. Eruption modeling and petrological analyses (e.g. Larsen et al., 2013; Biggs et
 286 al., 2016), which are outside the scope of this study, would help examine this phenomenon of
 287 successive tapping of two reservoirs during the eruption. The conduits or fractures produced
 288 by the explosive eruption of the L2 reservoir would make it easy for the magma in the L1
 289 reservoir to flow out. Nevertheless, the lateral transport of magma is commonly seen or
 290 proposed at other volcanoes (e.g., Tibaldi, 2015; Lerner et al., 2020; Kiser et al., 2021). A
 291 more detailed seismic imaging with improved station coverage is required to narrow down
 292 the explanations.

293 ***Stage-6: Resurgence of the deeper L2 reservoir.*** As the eruption becomes more
 294 effusive and dome emplacement slows down, magmatic activity switches back to the deeper

295 L2 reservoir. This is supported by a cluster of small earthquakes below the L2 reservoir
296 (swarm-3), overall deeper than swarm-1 earthquakes. The magma activity in the L1 reservoir
297 decays during this stage. Stages 3-6 involve a model of two active reservoirs that alternate
298 as sources of the eruption.

299 4.4 Future studies

300 With two magma reservoirs, migrating volcanic seismicity, and a collapsed caldera,
301 Great Sitkin Volcano provides an ideal natural laboratory to study the dynamics of magma
302 plumbing systems and volcanic hazards. Due to the limited data coverage, there are several
303 remaining questions to be addressed by future studies about the eruption dynamics at Great
304 Sitkin with multi-disciplinary observations. A better constraint on the lateral and depth
305 scales of the L2 reservoir requires a larger aperture seismic array. Denser station coverage
306 is needed to image the distribution of shallow magma conduits below the summit and to
307 understand their control of magma transport and the eruption explosivity. Data on surface
308 deformation (e.g., InSAR mapping) would help to examine the surface inflation and deflation
309 corresponding to different eruption stages. The record of surface temperature over the past
310 several years and its spatial distribution would help refine the temperature anomaly at
311 different stages as well as the estimate of melt fractions. Measurements of volatile emissions
312 from the volcano would also improve melt fraction estimates. In addition, a high-resolution
313 gravity survey is required to delineate the heterogeneity of density below the island.

314 5 Conclusions

315 The geometry and dynamics of magma plumbing systems play an essential role in
316 controlling the eruption behavior of active volcanoes. Furthermore, the distribution of
317 earthquakes provides essential insights into the magma transport below the volcano. At
318 Great Sitkin Volcano in the central Aleutian Arc, Alaska, which erupted on 26 May 2021
319 and continues with ongoing effusive lava flows, the seismicity patterns during the past two
320 decades show a strong migration across the volcanic island from northwest to southeast
321 of the edifice. Multiple swarms of earthquakes have occurred at different locations as the
322 eruption cycle evolved. We construct a 3-D crustal shear-wave velocity model of Great
323 Sitkin Island for the upper 6 km of the crust BSL, which reveals two low-velocity anomalies
324 corresponding to mushy magma reservoirs with up to approximately 30% partial melts. We
325 propose a six-stage eruption cycle to explain the migration of seismicity and the alternating
326 eruption of the two reservoirs with different recharging histories. The findings in this study
327 have broad implications for the dynamics of magma plumbing systems and the structural
328 control of eruption behavior.

329 Open Research

330 The seismic waveforms from the Alaska Volcano Observatory network (Alaska Vol-
331 cano Observatory/USGS, 1988) were downloaded from IRIS Data Management Center
332 (<https://ds.iris.edu/ds/nodes/dmc/>) and processed using *SeisGo* (<https://doi.org/10.5281/zenodo.5873724>), built upon *ObsPy* (Beyreuther et al., 2010) and *NoisePy* (Jiang & Denolle, 2020).

335 Acknowledgments

336 This research has been funded by the startup funding of Purdue University for Xiaotao Yang.
337 **Author Contributions:** X. Yang contributed to conceptualization, supervision, funding
338 acquisition, data curation, methodology, formal analysis, interpretation, and writing of the
339 original draft. D. Roman, M. Haney, and C. Kupres all contributed to the interpretation
340 and reviewing and editing of the manuscript.

341 **References**

- 342 Alaska Volcano Observatory/USGS. (1988). *Alaska Volcano Observatory* (Tech. Rep.).
 343 Anchorage, AK: International Federation of Digital Seismograph Networks. doi: 10
 344 .7914/SN/AV
- 345 Avellaneda, M. (1987, 9). Iterated homogenization, differential effective medium the-
 346 ory and applications. *Communications on Pure and Applied Mathematics*, *40*,
 347 527-554. Retrieved from [https://onlinelibrary.wiley.com/doi/full/10.1002/](https://onlinelibrary.wiley.com/doi/full/10.1002/cpa.3160400502)
 348 [cpa.3160400502](https://onlinelibrary.wiley.com/doi/full/10.1002/cpa.3160400502) doi: 10.1002/CPA.3160400502
- 349 Barker, S. E., & Malone, S. D. (1991, 7). Magmatic system geometry at Mount St. Helens
 350 modeled from the stress field associated with post-eruptive earthquakes. *Journal of*
 351 *Geophysical Research*, *96*, 11883. Retrieved from [http://doi.wiley.com/10.1029/](http://doi.wiley.com/10.1029/91JB00430)
 352 [91JB00430](http://doi.wiley.com/10.1029/91JB00430) doi: 10.1029/91JB00430
- 353 Bensen, G. D., Ritzwoller, M. H., Barmin, M. P., Levshin, A. L., Lin, F., Moschetti, M. P.,
 354 ... Yang, Y. (2007). Processing seismic ambient noise data to obtain reliable broad-
 355 band surface wave dispersion measurements. *Geophysical Journal International*, *169*,
 356 1239-1260. doi: 10.1111/j.1365-246X.2007.03374.x
- 357 Benz, H. M., Chouet, B. A., Dawson, P. B., Lahr, J. C., Page, R. A., & Hole, J. A.
 358 (1996, 4). Three-dimensional *P* and *S* wave velocity structure of Redoubt Volcano,
 359 Alaska. *Journal of Geophysical Research: Solid Earth*, *101*, 8111-8128. Retrieved
 360 from <http://doi.wiley.com/10.1029/95JB03046> doi: 10.1029/95JB03046
- 361 Berryman, J. G. (1998, 6). Long-wavelength propagation in composite elastic media ii.
 362 ellipsoidal inclusions. *The Journal of the Acoustical Society of America*, *68*, 1820.
 363 Retrieved from <https://asa.scitation.org/doi/abs/10.1121/1.385172> doi: 10
 364 .1121/1.385172
- 365 Beyreuther, M., Barsch, R., Krischer, L., Megies, T., Behr, Y., & Wassermann, J. (2010,
 366 05). ObsPy: A Python Toolbox for Seismology. *Seismological Research Letters*, *81*(3),
 367 530-533. Retrieved from <https://doi.org/10.1785/gssrl.81.3.530> doi: 10.1785/
 368 gssrl.81.3.530
- 369 Biggs, J., Robertson, E., & Cashman, K. (2016, 4). The lateral extent of volcanic interactions
 370 during unrest and eruption. *Nature Geoscience*, *9*, 308-311. Retrieved from [http://](http://www.nature.com/articles/ngeo2658)
 371 www.nature.com/articles/ngeo2658 doi: 10.1038/ngeo2658
- 372 Chaussard, E., Amelung, F., & Aoki, Y. (2013, 8). Characterization of open and
 373 closed volcanic systems in Indonesia and Mexico using InSAR time series. *Jour-*
 374 *nal of Geophysical Research: Solid Earth*, *118*, 3957-3969. Retrieved from
 375 <https://onlinelibrary.wiley.com/doi/full/10.1002/jgrb.50288>
 376 [https://](https://onlinelibrary.wiley.com/doi/full/10.1002/jgrb.50288)
 377 onlinelibrary.wiley.com/doi/10.1002/jgrb.50288 doi: 10.1002/JGRB.50288
- 378 Christensen, N. L., & Stanley, D. (2003). Seismic velocities and densities of rocks. *Internat-*
 379 *ional Geophysics*, *81*, 1587-1594. doi: 10.1016/S0074-6142(03)80278-4
- 380 Chu, R., Helmberger, D. V., Sun, D., Jackson, J. M., & Zhu, L. (2010, 1). Mushy magma
 381 beneath yellowstone. *Geophysical Research Letters*, *37*. doi: 10.1029/2009GL041656
- 382 Delph, J. R., Ward, K. M., Zandt, G., Ducea, M. N., & Beck, S. L. (2017). Imaging a
 383 magma plumbing system from mash zone to magma reservoir. *Earth and Planetary*
 384 *Science Letters*, *457*, 313-324. Retrieved from www.elsevier.com/locate/epsl doi:
 385 10.1016/j.epsl.2016.10.008
- 386 Fischer, T. P., Arellano, S., Carn, S., Aiuppa, A., Galle, B., Allard, P., ... Chiodini,
 387 G. (2019, 12). The emissions of CO₂ and other volatiles from the world's subaerial
 388 volcanoes. *Scientific Reports* *2019 9:1*, *9*, 1-11. Retrieved from [https://www.nature](https://www.nature.com/articles/s41598-019-54682-1)
 389 [.com/articles/s41598-019-54682-1](https://www.nature.com/articles/s41598-019-54682-1) doi: 10.1038/s41598-019-54682-1
- 390 Fischer, T. P., Lopez, T. M., Aiuppa, A., Rizzo, A. L., Ilanko, T., Kelley, K. A., & Cottrell,
 391 E. (2021, 12). Gas emissions from the western Aleutians volcanic arc. *Frontiers in*
 392 *Earth Science*, *9*, 1205. Retrieved from [https://www.frontiersin.org/articles/](https://www.frontiersin.org/articles/10.3389/feart.2021.786021/full)
 393 [10.3389/feart.2021.786021](https://www.frontiersin.org/articles/10.3389/feart.2021.786021/full) doi: 10.3389/feart.2021.786021
- 394 Flinders, A. F., & Shen, Y. (2017, 12). Seismic evidence for a possible deep crustal hot
 395 zone beneath southwest Washington. *Scientific Reports*, *7*, 7400. Retrieved from

- 396 <http://www.nature.com/articles/s41598-017-07123-w> doi: 10.1038/s41598-017-
397 -07123-w
- 398 Gao, H., & Shen, Y. (2012). Validation of shear-wave velocity models of the Pacific
399 Northwest. *Bulletin of the Seismological Society of America*, *102*, 2611-2621. doi:
400 10.1785/01201110336
- 401 Gao, H., & Shen, Y. (2014). Upper mantle structure of the Cascades from full-wave
402 ambient noise tomography: Evidence for 3d mantle upwelling in the back-arc. *Earth
403 and Planetary Science Letters*, *390*, 222-233. doi: 10.1016/j.epsl.2014.01.012
- 404 Global Volcanism Program. (2022a, May). *Report on Great Sitkin (United States)* (Vol. 47)
405 (No. 5). Smithsonian Institution.
- 406 Global Volcanism Program. (2022b, September). *Report on Great Sitkin (United States)*
407 (Vol. 43) (No. 9). Smithsonian Institution. Retrieved from [https://doi.org/10
408 .5479/si.GVP.BGVN201809-311120](https://doi.org/10.5479/si.GVP.BGVN201809-311120)
- 409 Huang, H. H., Lin, F. C., Schmandt, B., Farrell, J., Smith, R. B., & Tsai, V. C. (2015). The
410 Yellowstone magmatic system from the mantle plume to the upper crust. *Science*,
411 *348*, 773-776. doi: 10.1126/science.aaa5648
- 412 Ito, K. (1990, 1). Effects of H₂O on elastic wave velocities in ultrabasic rocks at 900°C
413 under 1 GPa. *Physics of the Earth and Planetary Interiors*, *61*, 260-268. Retrieved
414 from <https://linkinghub.elsevier.com/retrieve/pii/003192019090110J> doi:
415 10.1016/0031-9201(90)90110-J
- 416 Jaxybulatov, K., Shapiro, N. M., Koulakov, I., Mordret, A., Landes, M., & Sens-Schonfelder,
417 C. (2014, 10). A large magmatic sill complex beneath the Toba caldera. *Science*,
418 *346*, 617-619. Retrieved from [https://www.sciencemag.org/lookup/doi/10.1126/
419 science.1258582](https://www.sciencemag.org/lookup/doi/10.1126/science.1258582) doi: 10.1126/science.1258582
- 420 Jiang, C., & Denolle, M. A. (2020). Noisepy: A new high-performance
421 python tool for ambient-noise seismology. *Seismological Research Letters*.
422 Retrieved from [https://pubs.geoscienceworld.org/ssa/srl/article/583390/
423 NoisePy-A-New-HighPerformance-Python-Tool-for](https://pubs.geoscienceworld.org/ssa/srl/article/583390/NoisePy-A-New-HighPerformance-Python-Tool-for) doi: 10.1785/0220190364
- 424 Kern, H., Popp, T., Gorbatshevich, F., Zharikov, A., Lobanov, K., & Smirnov, Y. (2001,
425 8). Pressure and temperature dependence of v_p and v_s in rocks from the su-
426 perdeep well and from surface analogues at kola and the nature of velocity anisotropy.
427 *Tectonophysics*, *338*, 113-134. Retrieved from [https://linkinghub.elsevier.com/
428 retrieve/pii/S0040195101001287](https://linkinghub.elsevier.com/retrieve/pii/S0040195101001287) doi: 10.1016/S0040-1951(01)00128-7
- 429 Kiser, E., Levander, A., Schmandt, B., & Hansen, S. (2021, 3). Seismic evidence
430 of bottom-up crustal control on volcanism and magma storage near Mount St.
431 Helens. *Geophysical Research Letters*, *48*, e2020GL090612. Retrieved from
432 [https://onlinelibrary.wiley.com/doi/full/10.1029/2020GL090612https://
433 onlinelibrary.wiley.com/doi/abs/10.1029/2020GL090612https://agupubs
434 .onlinelibrary.wiley.com/doi/10.1029/2020GL090612](https://onlinelibrary.wiley.com/doi/full/10.1029/2020GL090612https://onlinelibrary.wiley.com/doi/abs/10.1029/2020GL090612https://agupubs) doi: 10.1029/
435 2020GL090612
- 436 Kiser, E., Palomeras, I., Levander, A., Zelt, C., Harder, S., Schmandt, B., ... Ulberg, C.
437 (2016). Magma reservoirs from the upper crust to the moho inferred from high-
438 resolution v_p and v_s models beneath Mount St. Helens, Washington State, USA.
439 *GEOLOGY*, *44*. Retrieved from www.geosociety.org/pubs/ft2016.htm, doi: 10
440 .1130/G37591.1
- 441 Korger, E., & Schlindwein, V. (2014, 1). Seismicity and structure of the
442 85°E volcanic complex at the ultraslow spreading Gakkel Ridge from lo-
443 cal earthquake tomography. *Geophysical Journal International*, *196*, 539-
444 551. Retrieved from [http://academic.oup.com/gji/article/196/1/539/592594/
445 Seismicity-and-structure-of-the-85E-volcanic](http://academic.oup.com/gji/article/196/1/539/592594/Seismicity-and-structure-of-the-85E-volcanic) doi: 10.1093/gji/ggt390
- 446 Larsen, J. F., Śliwiński, M. G., Nye, C., Cameron, C., & Schaefer, J. R. (2013, 8). The 2008
447 eruption of Okmok Volcano, Alaska: Petrological and geochemical constraints on the
448 subsurface magma plumbing system. *Journal of Volcanology and Geothermal Research*,
449 *264*, 85-106. Retrieved from [https://linkinghub.elsevier.com/retrieve/pii/
450 S0377027313002217](https://linkinghub.elsevier.com/retrieve/pii/S0377027313002217) doi: 10.1016/j.jvolgeores.2013.07.003

- 451 Lees, J. M. (2007, 11). Seismic tomography of magmatic systems. *Journal of Volcanology and*
 452 *Geothermal Research*, *167*, 37-56. Retrieved from [https://linkinghub.elsevier](https://linkinghub.elsevier.com/retrieve/pii/S0377027307001965)
 453 [.com/retrieve/pii/S0377027307001965](https://linkinghub.elsevier.com/retrieve/pii/S0377027307001965) doi: 10.1016/j.jvolgeores.2007.06.008
- 454 Lerner, A. H., O'Hara, D., Karlstrom, L., Ebmeier, S. K., Anderson, K. R., & Hurwitz, S.
 455 (2020, 7). The prevalence and significance of offset magma reservoirs at arc volcanoes.
 456 *Geophysical Research Letters*, *47*. Retrieved from [https://onlinelibrary.wiley](https://onlinelibrary.wiley.com/doi/10.1029/2020GL087856)
 457 [.com/doi/10.1029/2020GL087856](https://onlinelibrary.wiley.com/doi/10.1029/2020GL087856) doi: 10.1029/2020GL087856
- 458 Lin, G., Shearer, P. M., Matoza, R. S., Okubo, P. G., & Amelung, F. (2014, 5).
 459 Three-dimensional seismic velocity structure of Mauna Loa and Kilauea volcanoes
 460 in Hawaii from local seismic tomography. *Journal of Geophysical Research: Solid*
 461 *Earth*, *119*, 4377-4392. Retrieved from [https://onlinelibrary.wiley.com/](https://onlinelibrary.wiley.com/doi/full/10.1002/2013JB010820)
 462 [doi/full/10.1002/2013JB010820](https://onlinelibrary.wiley.com/doi/full/10.1002/2013JB010820)[https://onlinelibrary.wiley.com/doi/](https://onlinelibrary.wiley.com/doi/abs/10.1002/2013JB010820)
 463 [abs/10.1002/2013JB010820](https://agupubs.onlinelibrary.wiley.com/doi/abs/10.1002/2013JB010820)[https://agupubs.onlinelibrary.wiley.com/doi/](https://agupubs.onlinelibrary.wiley.com/doi/10.1002/2013JB010820)
 464 [10.1002/2013JB010820](https://agupubs.onlinelibrary.wiley.com/doi/10.1002/2013JB010820) doi: 10.1002/2013JB010820
- 465 Loewen, M. W. (2021). *Thin section crossed-polarized light photomicrograph of a radial pla-*
 466 *gioclase phenocryst in a May 25, 2021, Great Sitkin breadcrust bomb*. Alaska Volcano
 467 Observatory / U.S. Geological Survey. Retrieved from [https://avo.alaska.edu/](https://avo.alaska.edu/images/image.php?id=178421)
 468 [images/image.php?id=178421](https://avo.alaska.edu/images/image.php?id=178421)
- 469 Marchese, F., & Genzano, N. (2022, 10). Global volcano monitoring through the Nor-
 470 malized Hotspot Indices (NHI) system. *Journal of the Geological Society*. Re-
 471 trieved from <https://www.lyellcollection.org/doi/10.1144/jgs2022-014> doi:
 472 10.1144/jgs2022-014
- 473 Miller, T. P., McGimsey, R. G., Richter, D. H., Riehle, J. R., Nye, C., Yount, M. E.,
 474 & Dumoulin, J. A. (1998). Catalog of the historically active volcanoes of Alaska.
 475 *Open-File Report*. doi: 10.3133/OFR98582
- 476 Norris, A. (1985, 3). A differential scheme for the effective moduli of composites. *Me-*
 477 *chanics of Materials*, *4*, 1-16. Retrieved from [https://linkinghub.elsevier.com/](https://linkinghub.elsevier.com/retrieve/pii/016766368590002X)
 478 [retrieve/pii/016766368590002X](https://linkinghub.elsevier.com/retrieve/pii/016766368590002X) doi: 10.1016/0167-6636(85)90002-X
- 479 Patanè, D., Barberi, G., Gori, P. D., Cocina, O., Zuccarello, L., Garcia-Yeguas, A., ...
 480 Sgroi, T. (2017, 7). The shallow magma chamber of Stromboli Volcano (Italy). *Geo-*
 481 *physical Research Letters*, *44*, 6589-6596. Retrieved from [https://onlinelibrary](https://onlinelibrary.wiley.com/doi/full/10.1002/2017GL073008)
 482 [.wiley.com/doi/full/10.1002/2017GL073008](https://onlinelibrary.wiley.com/doi/full/10.1002/2017GL073008) doi: 10.1002/2017GL073008
- 483 Paulatto, M., Hooft, E. E. E., Chrapkiewicz, K., Heath, B., Toomey, D. R., & Morgan, J. V.
 484 (2022, 10). Advances in seismic imaging of magma and crystal mush. *Frontiers in*
 485 *Earth Science*, *10*, 2005. Retrieved from [https://www.frontiersin.org/articles/](https://www.frontiersin.org/articles/10.3389/feart.2022.970131/full)
 486 [10.3389/feart.2022.970131/full](https://www.frontiersin.org/articles/10.3389/feart.2022.970131/full) doi: 10.3389/feart.2022.970131
- 487 Pesicek, J. D., Thurber, C. H., DeShon, H. R., Prejean, S. G., & Zhang, H. (2008, 10). Three-
 488 Dimensional P-Wave Velocity Structure and Precise Earthquake Relocation at Great
 489 Sitkin Volcano, Alaska. *Bulletin of the Seismological Society of America*, *98*, 2428-
 490 2448. Retrieved from [https://pubs.geoscienceworld.org/bssa/article/98/5/](https://pubs.geoscienceworld.org/bssa/article/98/5/2428-2448/350147)
 491 [2428-2448/350147](https://pubs.geoscienceworld.org/bssa/article/98/5/2428-2448/350147) doi: 10.1785/0120070213
- 492 Power, J. A., Stihler, S., White, R., & Moran, S. (2004, 12). Observations of deep long-period
 493 (DLP) seismic events beneath Aleutian arc volcanoes; 1989-2002. *Journal of Volcanol-*
 494 *ogy and Geothermal Research*, *138*, 243-266. Retrieved from [https://linkinghub](https://linkinghub.elsevier.com/retrieve/pii/S0377027304002392)
 495 [.elsevier.com/retrieve/pii/S0377027304002392](https://linkinghub.elsevier.com/retrieve/pii/S0377027304002392) doi: 10.1016/j.jvolgeores.2004
 496 .07.005
- 497 Power, J. A., Villaseñor, A., & Benz, H. M. (1998). Seismic image of the Mount Spurr
 498 magmatic system. *Bulletin of Volcanology*, *60*, 27-37. doi: 10.1007/s004450050214
- 499 Roman, D. C., & Cashman, K. V. (2018, 9). Top-down precursory volcanic seismicity:
 500 Implications for 'stealth' magma ascent and long-term eruption forecasting. *Frontiers*
 501 *in Earth Science*, *6*, 124. doi: 10.3389/FEART.2018.00124/BIBTEX
- 502 Roman, D. C., Power, J. A., Moran, S. C., Cashman, K. V., Doukas, M. P., Neal,
 503 C. A., & Gerlach, T. M. (2004, 2). Evidence for dike emplacement beneath Il-
 504 liamna Volcano, Alaska in 1996. *Journal of Volcanology and Geothermal Research*,
 505 *130*, 265-284. Retrieved from <https://linkinghub.elsevier.com/retrieve/pii/>

- 506 S0377027303003020 doi: 10.1016/S0377-0273(03)00302-0
- 507 Scandone, R., Cashman, K. V., & Malone, S. D. (2007). Magma supply, magma ascent
508 and the style of volcanic eruptions. *Earth and Planetary Science Letters*, *253*(3),
509 513-529. Retrieved from [https://www.sciencedirect.com/science/article/pii/](https://www.sciencedirect.com/science/article/pii/S0012821X06008181)
510 [S0012821X06008181](https://www.sciencedirect.com/science/article/pii/S0012821X06008181) doi: <https://doi.org/10.1016/j.epsl.2006.11.016>
- 511 Shapiro, N. M., & Ritzwoller, M. H. (2002). Monte-Carlo inversion for a global shear-velocity
512 model of the crust and upper mantle. *Geophysical Journal International*, *151*, 88-105.
513 doi: 10.1046/j.1365-246X.2002.01742.x
- 514 Sparks, R. S. J., Annen, C., Blundy, J. D., Cashman, K. V., Rust, A. C., & Jackson,
515 M. D. (2019, 2). Formation and dynamics of magma reservoirs. *Philosophical*
516 *Transactions of the Royal Society A: Mathematical, Physical and Engineering Sci-*
517 *ences*, *377*, 20180019. Retrieved from [https://royalsocietypublishing.org/doi/](https://royalsocietypublishing.org/doi/10.1098/rsta.2018.0019)
518 [10.1098/rsta.2018.0019](https://royalsocietypublishing.org/doi/10.1098/rsta.2018.0019) doi: 10.1098/rsta.2018.0019
- 519 Spera, F. J. (2004, 8). Open-system magma chamber evolution: an energy-constrained geo-
520 chemical model incorporating the effects of concurrent eruption, recharge, variable as-
521 similation and fractional crystallization (EC-E'RA χ C). *Journal of Petrology*, *45*, 2459-
522 2480. Retrieved from [https://academic.oup.com/petrology/article-lookup/](https://academic.oup.com/petrology/article-lookup/doi/10.1093/petrology/egh072)
523 [doi/10.1093/petrology/egh072](https://academic.oup.com/petrology/article-lookup/doi/10.1093/petrology/egh072) doi: 10.1093/petrology/egh072
- 524 Takei, Y. (2002, 2). Effect of pore geometry on V_P/V_S : From equilibrium
525 geometry to crack. *Journal of Geophysical Research: Solid Earth*, *107*,
526 ECV 6-1. Retrieved from [https://onlinelibrary.wiley.com/doi/full/](https://onlinelibrary.wiley.com/doi/full/10.1029/2001JB000522)
527 [10.1029/2001JB000522](https://onlinelibrary.wiley.com/doi/full/10.1029/2001JB000522)[https://onlinelibrary.wiley.com/doi/abs/10.1029/](https://onlinelibrary.wiley.com/doi/abs/10.1029/2001JB000522)
528 [2001JB000522](https://onlinelibrary.wiley.com/doi/abs/10.1029/2001JB000522)[https://agupubs.onlinelibrary.wiley.com/doi/10.1029/](https://agupubs.onlinelibrary.wiley.com/doi/10.1029/2001JB000522)
529 [2001JB000522](https://agupubs.onlinelibrary.wiley.com/doi/10.1029/2001JB000522) doi: 10.1029/2001JB000522
- 530 Tibaldi, A. (2015, 6). Structure of volcano plumbing systems: A review of multi-parametric
531 effects. *Journal of Volcanology and Geothermal Research*, *298*, 85-135. doi: 10.1016/
532 [J.JVOLGEORES.2015.03.023](https://doi.org/10.1016/J.JVOLGEORES.2015.03.023)
- 533 Ueki, K., & Iwamori, H. (2016, 5). Density and seismic velocity of hydrous melts
534 under crustal and upper mantle conditions. *Geochemistry, Geophysics, Geosys-*
535 *tems*, *17*, 1799-1814. Retrieved from [https://onlinelibrary.wiley.com/](https://onlinelibrary.wiley.com/doi/full/10.1002/2015GC006242)
536 [doi/full/10.1002/2015GC006242](https://onlinelibrary.wiley.com/doi/full/10.1002/2015GC006242)[https://onlinelibrary.wiley.com/doi/](https://onlinelibrary.wiley.com/doi/abs/10.1002/2015GC006242)
537 [abs/10.1002/2015GC006242](https://onlinelibrary.wiley.com/doi/abs/10.1002/2015GC006242)[https://agupubs.onlinelibrary.wiley.com/doi/](https://agupubs.onlinelibrary.wiley.com/doi/10.1002/2015GC006242)
538 [10.1002/2015GC006242](https://agupubs.onlinelibrary.wiley.com/doi/10.1002/2015GC006242) doi: 10.1002/2015GC006242
- 539 U.S. Geological Survey. (2022). *ANSS Comprehensive Earthquake Catalog* (Tech. Rep.).
540 Menlo Park, CA: U.S. Geological Survey.
- 541 Viens, L., Denolle, M., Miyake, H., Sakai, S., & Nakagawa, S. (2017, 7). Retrieving im-
542 pulse response function amplitudes from the ambient seismic field. *Geophysical Jour-*
543 *nal International*, *210*, 210-222. Retrieved from [https://academic.oup.com/gji/](https://academic.oup.com/gji/article-lookup/doi/10.1093/gji/ggx155)
544 [article-lookup/doi/10.1093/gji/ggx155](https://academic.oup.com/gji/article-lookup/doi/10.1093/gji/ggx155) doi: 10.1093/gji/ggx155
- 545 Ward, K. M., Delph, J. R., Zandt, G., Beck, S. L., & Ducea, M. N. (2017, 12). Magmatic
546 evolution of a cordilleran flare-up and its role in the creation of silicic crust. *Scientific*
547 *Reports*, *7*, 9047. Retrieved from [http://www.nature.com/articles/s41598-017-](http://www.nature.com/articles/s41598-017-09015-5)
548 [09015-5](http://www.nature.com/articles/s41598-017-09015-5) doi: 10.1038/s41598-017-09015-5
- 549 Waythomas, C. F., Miller, T. P., & Nye, C. (2003). Preliminary geologic map of Great
550 Sitkin Volcano, Alaska. *USGS Open-File Report*. Retrieved from [https://doi.org/](https://doi.org/10.3133/ofr0336)
551 [10.3133/ofr0336](https://doi.org/10.3133/ofr0336) doi: 10.3133/ofr0336
- 552 Yang, X., & Gao, H. (2018). Full-wave seismic tomography in the northeastern United
553 States: New insights into the uplift mechanism of the Adirondack Mountains. *Geo-*
554 *physical Research Letters*, *45*. doi: 10.1029/2018GL078438
- 555 Yang, X., & Gao, H. (2020). Segmentation of the Aleutian-Alaska subduction zone revealed
556 by full-wave ambient noise tomography: Implications for the along-strike variation of
557 volcanism. *Journal of Geophysical Research: Solid Earth*, *125*, 1-20. doi: 10.1029/
558 [2020JB019677](https://doi.org/10.1029/2020JB019677)
- 559 Yang, X., Zuffoletti, I. D., D'Souza, N. J., & Denolle, M. A. (2022, 1). *SeisGo: A ready-to-*
560 *go Python toolbox for seismic data analysis* [Computer Software]. Zenodo. Retrieved

561 from <https://doi.org/10.5281/zenodo.5873724> doi: 10.5281/zenodo.5873724
562 Zhang, W., Zhang, Z., & Chen, X. (2012). Three-dimensional elastic wave numerical
563 modelling in the presence of surface topography by a collocated-grid finite-difference
564 method on curvilinear grids. *Geophysical Journal International*, 190, 358-378. doi:
565 10.1111/j.1365-246X.2012.05472.x
566 Zhang, Z., & Shen, Y. (2008). Cross-dependence of finite-frequency compressional waveforms
567 to shear seismic wave speeds. *Geophysical Journal International*, 174, 941-948. doi:
568 10.1111/j.1365-246X.2008.03840.x